photonics

MDPI

Article

Comparison of Two- and Three-Beam Interference Pattern Generation in Structured Illumination Microscopy

Jiuling Liao [1,2], Lina Liu [1,2], Tingai Chen [1,2], Xianyuan Xia [1,2], Hui Li [1,2] and Wei Zheng [1,2,*]

[1] Research Center for Biomedical Optics and Molecular Imaging, Shenzhen Key Laboratory for Molecular Imaging, Guangdong Provincial Key Laboratory of Biomedical Optical Imaging Technology, Shenzhen Institutes of Advanced Technology, Chinese Academy of Sciences, Shenzhen 518055, China; jl.liao@siat.ac.cn (J.L.); lina.liu@siat.ac.cn (L.L.); cntgai@163.com (T.C.); xy.xia@siat.ac.cn (X.X.); hui.li@siat.ac.cn (H.L.)

[2] CAS Key Laboratory of Health Informatics, Shenzhen Institutes of Advanced Technology, Chinese Academy of Sciences, Shenzhen 518055, China

* Correspondence: zhengwei@siat.ac.cn

Abstract: Structured illumination microscopy (SIM) provides wide-field optical sectioning in the focal plane by modulating the imaging information using fringe pattern illumination. For generating the fringe pattern illumination, a digital micro-mirror device (DMD) is commonly used due to its flexibility and fast refresh rate. However, the benefit of different pattern generation, for example, the two-beam interference mode and the three-beam interference mode, has not been clearly investigated. In this study, we systematically analyze the optical sectioning provided by the two-beam inference mode and the three-beam interference mode of DMD. The theoretical analysis and imaging results show that the two-beam interference mode is suitable for fast imaging of the superficial dynamic target due to reduced number of phase shifts needed to form the image, and the three-beam interference mode is ideal for imaging three-dimensional volume due to its superior optical sectioning by the improved modulation of the illumination patterns. These results, we believe, will provide better guidance for the use of DMD for SIM imaging and also for the choice of beam patterns in SIM application in the future.

Keywords: structured illumination microscopy; optical sectioning; digital micro-mirror device; multi-beam interference

Citation: Liao, J.; Liu, L.; Chen, T.; Xia, X.; Li, H.; Zheng, W. Comparison of Two- and Three-Beam Interference Pattern Generation in Structured Illumination Microscopy. *Photonics* **2021**, *8*, 526. https://doi.org/10.3390/photonics8120526

Received: 23 September 2021
Accepted: 20 November 2021
Published: 23 November 2021

1. Introduction

Fluorescence microscopy with optical sectioning provides unique benefits for the biological studies. Among fluorescence optical sectioning techniques, such as confocal laser scanning microscopy (CLSM) [1], two-photon microscopy (2PM) [2], and light-sheet fluorescence microscopy (LSFM) [3], structured illumination microscopy (SIM) is of growing interest due to its ability to easily integrate wide-field microscope and the high-speed 3D imaging capability [4,5]. In SIM, the specimen is illuminated by a predefined periodic excitation pattern. Only at the focus, the information is modulated by this illumination fringe while rapidly attenuating beyond the focus area. An optical sectioning image is reconstructed by a series of raw images obtained from the illumination patterns obtained in equal phase steps. Compared to the point-by-point scanning approaches, such as CLSM and 2PM, SIM provides higher-speed image acquisition because of its wide-field operating mode.

The SIM has progressed through several advances over the years, specifically with respect to exciting the specimen with high-contrast, fine illumination patterns for obtaining high-quality images. In early years, a grating was usually used to generate the illumination patterns [6]. The grating was mechanically rotated or translated to obtain different patterns, thus the process was quite slow. Later, new opto-electro devices, such as the liquid crystal

spatial light modulator (SLM) [4] and the digital micro-mirror device (DMD) which could be considered as a fast programmable grating [7], were applied to raise the switching speed of the fringe patterns. Compared to the SLM, which offers a refresh rate of hundreds of Hz, DMD is capable of refresh rate of up to 32.5 kHz [8]. Thus, the use of DMD in SIM has attracted much attention in the past decade.

In DMD-based SIM systems (DMD-SIM), there are two major approaches to project fringe pattern: first is the direct projection of the pattern displayed on DMD, and the second is adopting the interference patterns for coherent light illumination. The first approach is suitable for incoherent illumination microscopy [9,10]. In the second approach, the DMD works as a diffraction grating, and its diffractive beams produce an interference pattern on the sample plane [7]. Although the incoherent light, such as an LED, was used in the early SIM systems, the adoption of coherent light, such as a laser, has become more attractive due to high brightness and high beam quality. Therefore, the interference approach has attracted much attention in the past decades.

In the interference approach, previous studies usually used two-beam interference ($\pm$1st order) to generate the illumination patterns for coherent illumination [7]. However, Gustafsson et al. pointed out that three-beam interference (0th, $\pm$1st order) can also form a periodical pattern for structured illumination [11,12]. Although the three-beam interference is widely used for super-resolution SIM image, its potential for optical sectioning SIM imaging has not been excavated. Furthermore, the comparison of the optical sectioning performance between two-beam interference [13] and three-beam interference [14] in SIM has not yet been investigated systematically.

This study compares the fringe pattern difference between the two-beam and three-beam interference and analyzes their influence on optical sectioning both in theory and experiment. The measured axial FWHMs in experiments for different pattern periods agree with the theoretical prediction. We found the two-beam interference mode is suitable for fast imaging of the superficial dynamic target, whereas the three-beam interference mode is beneficial for imaging three-dimensional volume due to its superior optical sectioning capability.

2. Theory

2.1. The Excitation Fringe Patterns Formed by Two-Beam and Three-Beam Interference

On the sample plane, shown in Figure 1a, the sample is illuminated by different coherent diffraction beams generated from DMD. For simplicity, the impact of polarization on the fringe contrast was ignored. We assume the periodic pattern is distributed in the x direction. The θ is the angle between the 0th and $\pm$1st order beams. In our paper, this angle is determined by the magnification of the optical system and the period of the stripes pattern displayed on the DMD. The complex amplitude of the $\pm$1st and 0th order diffraction light on the sample plane is $A_{+1} = Ae^{i\delta}$, $A_{-1} = Ae^{-i\delta}$, $A_0 = \varepsilon Ae^{i0}$, respectively. Here, A is the amplitude, ε is the amplitude ratio between the 0th and $\pm$1st order beams, δ is the phase factor between the 0th and +1st order diffraction beam ($-\delta$ for the 0th and -1st order diffraction beam), and it is calculated using $\delta = k\Delta + \varphi$, where Δ is the optical path difference between the 0th and +1st order diffraction beam and can be approximated as $\Delta \approx x \sin\theta$, φ is an arbitrary spatial phase, and k is the angular wavenumber $k = 2\pi/\lambda$.

In the two-beam illumination case, the sample is illuminated by the interference pattern formed by $\pm$1st order diffraction beams. The coherent superposition of two-beam produces the excitation intensity as follows:

$$I_2 = |A_{+1} + A_{-1}|^2 = \left|Ae^{-i\delta} + Ae^{i\delta}\right|^2 = 4A^2\cos^2\delta = 2A^2(\cos 2\delta + 1) \quad (1)$$

If $\delta = m\pi$,$m = 0, \pm1, \pm2, \cdots$, the bright fringes with the maximum intensity value of $4A^2$ are formed. The period of fringe formed by two-beam interfering on the sample plane has the form

$$\Lambda_{s2} = \lambda/(2\sin\theta) \quad (2)$$

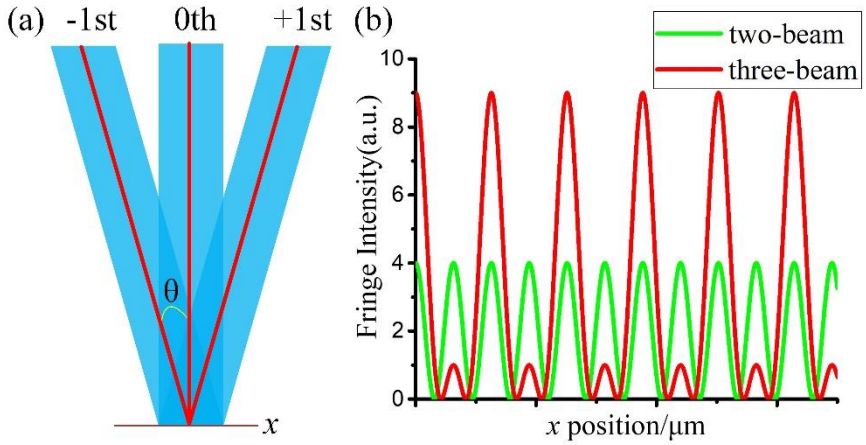

Figure 1. (**a**) Schematic diagram of three diffraction beams illumination on the sample plane. (**b**) The excitation intensity distributions along the x direction on the sample plane by two-beam (green) and three-beam (red) interference, assuming that the intensities of 0th and ±1st order diffraction beams are identical. The larger the incident angle, the denser the fringes on the sample plane.

Similarly, in the three-beam illumination case, the excitation intensity interfered by the 0th and the ±1st order diffraction beams can be written as

$$\begin{aligned} I_3 &= |A_{+1} + A_0 + A_{-1}|^2 = \left|Ae^{-i\delta} + \varepsilon A e^{i0} + Ae^{i\delta}\right|^2 \\ &= A^2(\varepsilon + 2\cos\delta)^2 = A^2(\varepsilon^2 + 2 + 4\varepsilon\cos\delta + 2\cos 2\delta). \end{aligned} \tag{3}$$

For simplicity, we assume the intensities of 0th and ±1st order diffraction beams to be identical ($\varepsilon = 1$). Thus, the intensity of the brightest interference fringe is $9A^2$ when δ satisfies $\delta = 2m\pi$, $m = 0, \pm 1, \pm 2, \cdots$. The period of fringe formed by three-beam interfering on the sample plane is expressed as

$$\Lambda_{s3} = \lambda / \sin\theta \tag{4}$$

As shown in Figure 1b, the two-beam interference has the brightest fringe of $4A^2$, whereas the three-beam interference has the brightest fringe of $9A^2$. From Equation (2) and (4), we can find that three-beam interference could result in sparser fringes than the two-beam interference. Therefore, the three-beam interference provides greater modulation contrast than that of two-beam interference.

2.2. The SIM Images Reconstructed from Two-Beam and Three-Beam Interference Illumination

When the sample is excited with interference fringes, the emission fluorescence I_{em} contains two parts: the weakly modulated out-of-focus component I_{de} and the information near the focal plane I_{in} with a predefined periodic excitation pattern P projected onto the focal plane. I_{em} can be written in the form

$$I_{em} = I_{de} + I_{in} \cdot P \tag{5}$$

In the two-beam illumination case, we substitute I_2 for P, and the Equation (5) can be written as

$$I_{em} = I_{de} + I_{in}(\cos 2\delta + 1) = I_{de} + I_{in} + I_{in}\cos 2\delta = I_0 + I_c \cos 2\varphi + I_s \sin 2\varphi \tag{6}$$

where I_c and I_s represent the images due to masks of forms $I_{in}\cos(2k\Delta)$ and $I_{in}\sin(2k\Delta)$, respectively. From these definitions, we can obtain the in-focus image by $I_{in} = \sqrt{{I_c}^2 + {I_s}^2}$. Considering there are three unknown parameters I_0, I_c, I_s, we should change the phase φ at least 3 steps ($\varphi = 0,\ 2\pi/3,\ 4\pi/3$) to calculate them. The phase shift of the fringe can be implemented easily by moving the fringes displayed on the DMD.

For three-beam illumination, I_{em} becomes

$$\begin{aligned} I_{em} &= I_{de} + I_{in}(3 + 4\cos\delta + 2\cos 2\delta) = I_{de} + 3I_{in} + 4I_{in}\cos\delta + 2I_{in}\cos 2\delta \\ &= I_0 + I_{c1}\cos\varphi + I_{s1}\sin\varphi + I_{c2}\cos 2\varphi + I_{s2}\sin 2\varphi \end{aligned} \quad (7)$$

where $I_{c1} = 4I_{in}\cos(k\Delta)$,$I_{s1} = 4I_{in}\sin(k\Delta)$,$I_{c2} = 2I_{in}\cos(2k\Delta)$,$I_{s2} = 2I_{in}\cos(2k\Delta)$. To solve five unknown parameters I_0, I_{c1}, I_{s1}, I_{c2}, I_{s2}, the phase φ is changed in at least 5 steps ($\varphi = 0$, $2\pi/5$, $4\pi/5$, $6\pi/5$, $8\pi/5$). This process is adapted from a previous study [11]. The in-focus image can be obtained by

$$I_{in} = \frac{1}{16}\sqrt{{I_{c1}}^2 + {I_{s1}}^2} \text{ or } I_{in} = \frac{1}{4}\sqrt{{I_{c2}}^2 + {I_{s2}}^2} \quad (8)$$

Generally, the wide-field and in-focus images are calculated by conventional SIM algorithm. The wide-field image is reconstructed by averaging all acquired raw images as follows [15]

$$I_{uniform} = \frac{1}{N}\sum_{1}^{N} I_N \quad (9)$$

and the in-focus image of fluorescent objects is reconstructed by

$$I_{reconstructed} = \left| \sum_{n=1}^{N} I_N \exp(i2\pi n/N) \right| \quad (10)$$

In summary, in the two-beam interference mode, the sample is illuminated by a sinusoidal light intensity pattern and has only three Fourier components. Therefore, three structured images are required to reconstruct an optical sectioning image. In contrast, in the three-beam interference mode, three diffractive beams superimpose to produce a three-dimensional excitation intensity pattern containing five Fourier components. Thus, it requires at least five images with phase-shifted illumination to reconstruct the optical sectioning image. Therefore, the two-beam interference mode provides a faster imaging rate compared with three-beam interference mode.

2.3. Assessment of the Optical Sectioning Capability

Optical sectioning is a process to distinguish in-focus information from the out-of-focus background, and it can usually be quantified by axial resolution, which is calculated from the full width at half maximum (FWHM) of axial intensity distribution (or known as an axial response) [12]. In DMD-SIM, the axial intensity distribution $I(z, v)$ can be expressed in the following formula with the Stokseth's approximation [16] as

$$I(z, v) \sim \left| 2\frac{J_1[uv(1 - v/2)]}{[uv(1 - v/2)]} \right| \quad (11)$$

where, $u = 8(\pi/\lambda)\sin^2(\alpha/2)\cdot z$, $v = \lambda/(\Lambda_S \cdot NA)$, $J_1(.)$ is the first-order Bessel function, u is the normalized defocus, z is the defocus variable, e.g., $z = 0$ means it is at the focal plane, v is the normalized spatial frequency, which is related to the period Λ_s of illumination fringe pattern, and NA is the numerical aperture of the objective lens, $NA = n\sin\alpha$ (n is refraction index, α is the half aperture angle of the objective lens). The Λ_S is related to the fringe period Λ_D, which is displayed on the DMD plane and will be discussed in the following chapter. Equation (11) can be applied to both two-beam and three-beam interference. In the case of $v = 0$, which corresponds to uniform illumination, $I(z) =$ constant and there is no sectioning effect. The optical sectioning strength can be defined as the FWHM of the $I(z, v)$ curve in DMD-SIM. From Equation (11), two roots $z_1 z_2$ can be calculated by solving $\left| 2\frac{J_1[uv(1-v/2)]}{[uv(1-v/2)]} \right| = \frac{1}{2}$. Thus we obtain FWHM, where [12]

$$\text{FWHM} = |z_1 - z_2| \quad (12)$$

3. Materials and Methods

3.1. Fluorescent Microspheres Sample Preparation

The thin fluorescent sheet was created through the following steps: (1) diluting a suspension of 40 nm microspheres (FluoSpheres® NeutrAvidin®-Labeled Microspheres, Thermo Fisher Scientific, Waltham, MA, USA) in water, (2) dropping the suspension on a slide, (3) covering the slide with a cover glass, and finally (4) sealing the edges with wax before it dried out. The thin fluorescent sheet was stored at 4 °C and protected from light until it was used.

The optical flow phantom model was constructed by pouring 15 μm microsphere (FluoSpheres® Polystyrene Microspheres, Thermo Fisher Scientific) dilute suspension into a 5 mL plastic syringe, which was fixed with a micro syringe pump (single channel syringe pump, Longer Precision Pump). The microsphere dilute suspension was then injected into a 0.5 mm internal diameter FEP tubing, part of it was sandwiched between two slides and fixed on the sample stage. By using a micro-syringe pump, the flow speed of fluorescent microspheres inside the FEP tubing was controlled appropriately.

3.2. Biological Sample Preparation

A Tg (Thy1-EGFP) MJrs/J mouse, approximately 4 weeks old, was deeply anesthetized with a mixture of 2% α-chloralose and 10% urethane (8 mL/kg) through intraperitoneal injection and perfused with 4% PFA/PBS transcardially. The whole brain was extracted and subjected overnight to post-fixation in 4% PFA. The optical clearing procedure is as following. After rinsing the brain several times with PBS, the post-fixed mouse brain was sliced into 500 μm coronal sections using a brain matrix. The sample was incubated in 10 mL optical clearing reagent [25 wt% urea, 25 wt% N,N,N′,N′-Tetrakis(2-hydroxypropyl) ethylenediamine and 15 wt% Triton X-100] and placed on a seesaw shaker for 1–2 h. The sample was then placed on a slide for repeat imaging.

All animal procedures were carried out in compliance with the laboratory animal protocols approved by the Institutional Animal Care and Use Committee of the Shenzhen Institutes of Advanced Technology, Chinese Academy of Sciences.

3.3. Structured Illumination Microscopy System Setup

The setup of our SIM system is shown in Figure 2. The excitation light (445 nm, 40 mw, from a diode-pumped solid-state laser system, CrystaLaser) is first coupled to a single-mode fiber (SM400, Thorlabs) to generate a collimated beam. The laser light exiting the fiber is collimated by the lens (L_1, f_1 = 75 mm) and sent to a pattern generator based on DMD (DLP Discovery4100, 1024×768 pixels, 13.68 μm×13.68 μm, Texas Instruments). To quickly switch periodic binary grating patterns on the DMD, we use the developed high speed DLP module, which is completely configurable by a high-speed FPGA logic and a USB 3.0 controller firmware, resulting in a switching rate up to 9.5 kHz. Each micro-mirror of the DMD can be moved independently into two states, "on" and "off", depending on whether the reflection goes to the light path ("on" state) or not ("off" state). Light modulated by the DMD is diffracted into different orders, mainly the 0th order and the ±1st orders. A relay lens (L_2, f_2 = 400 mm) focuses these diffraction orders into a mask plane, which is conjugate to the back focal plane of the objective. In this plane, a mask can be used to block out or not the 0th order, depending on two-beam or three-beam interference mode, respectively. After the diffracted beams pass through another relay lens (L_3, f_3 = 200 mm) and the tube lens (TL, f_{TL} = 175 mm), they are refocused onto the objective's back focal plane. The objective lens (PLN 10 × 0.25 NA, Olympus) then collimates diffracted beams, making them interfere to form a desired illumination pattern over the sample plane, which is a conjugate to the face of micro-mirror inside the DMD. We chose this objective lens ascribed to the purpose of ensuring a large field-of-view which is critical for the future clinical histological applications. The sample is fixed on a manual XY stage (XYFM1, Thorlabs), and the axial scanning is achieved by a compact motorized translation stage (MTS25-Z8, Thorlabs). Fluorescent light emitted from the sample is gathered by the same objective lens

and transmitted through the dichroic mirror (ZT442rdc, Chroma). A long-pass emission filter (HQ465lp, Chroma) was used to eliminate the residual excitation light. Finally, the image was captured by a scientific complementary metal-oxide-semiconductor camera (ORCA Flash4.0v2, 2048 × 2048 pixels, 6.5 µm × 6.5 µm, Hamamatsu) through a collection lens (L_4, f_4 = 300 mm).

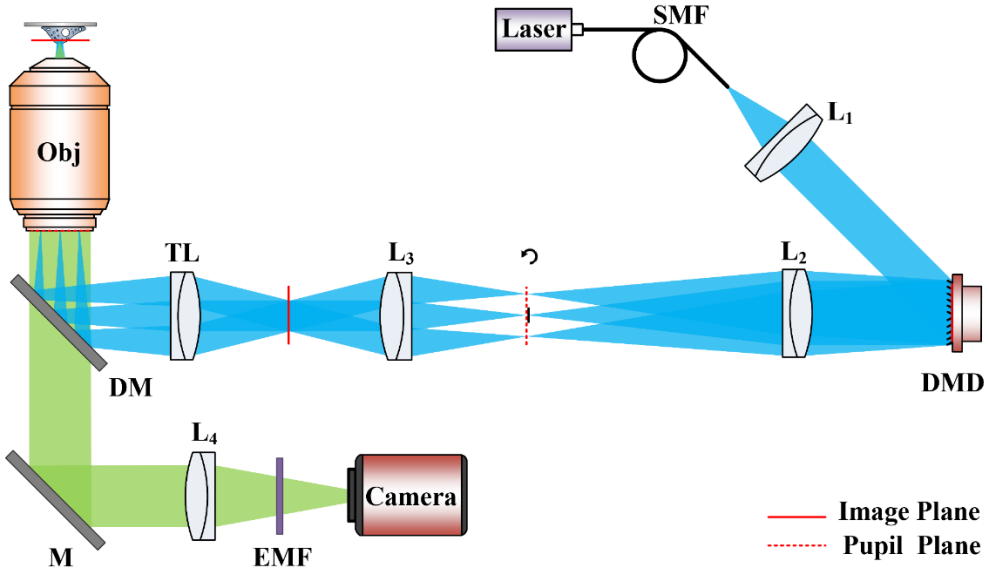

Figure 2. Schematic diagram of a fast structured illumination microscopy system setup. SMF: single-mode fiber; L: lens; TL: tube lens; DM: dichroic mirror; OBJ: objective; M: mirror; EMF: emission filter.

The synchronization between DMD, axial scanning stage, and the camera is achieved via a custom algorithm written in LabVIEW (National Instruments). The data acquisition was performed by an open-source platform in µ-manager. Binary grid patterns were first generated in a computer and uploaded to the on-board memory of DMD prior to displaying. The ORCA Flash4.0v2 sCMOS camera provides low noise and high-speed readout performance, thus is suitable for SIM imaging. In this study, the camera operated in external edge trigger mode. The exposure was triggered to start with the rising edge of the synchronization signal and the exposure time of the camera was set by commands in µ-manager. During the acquisition of each raw image, the same sample area was illuminated with a different pattern and the camera captures the displayed pattern. An axial scanning stage was used to control the imaging depth of the sample. Finally, a three-dimensional structure was reconstructed from a series of captured images.

As discussed above, the DMD was used as a diffraction grating for coherent light illumination. The incidence angle i and the diffraction angle θ_o satisfy the equation

$$\sin i + \sin \theta_o = \frac{m\lambda}{\Lambda_D} \tag{13}$$

According to Equation (13), the ±1st order diffraction angles, θ_{+1},θ_{-1} respectively, satisfy $\sin \theta_{+1} - \sin \theta_{-1} = 2\lambda/\Lambda_D$. Thus, after diffracted by the DMD, the angle θ_D between the 0th and ±1st order can be written as $\sin \theta_D = \lambda/\Lambda_D$. The relay lenses L_2 and L_3, tube lens and objective constitute two set of 4f systems. Thus,θ, the angle between the 0th and ±1st order beams on the sample plane, can be approximated by

$$\sin \theta = \beta \sin \theta_D = \frac{\beta\lambda}{\Lambda_D} \tag{14}$$

where β denotes the effective illumination magnification between the DMD plane to sample plane and is equal to the product of two 4f systems' magnification. By substituting the

$\sin\theta$ from Equation (14) into Equation (2) and Equation (4), the periods of two-beam and three-beam interference fringe patterns are obtained. The periods are $\Lambda_{S2} = \Lambda_D/2\beta$, $\Lambda_{S3} = \Lambda_D/\beta$, for two-beam and three-beam, respectively.

4. Results

4.1. Optical Sectioning Comparison between Two-Beam and Three-Beam Interference Mode

First, we examined the axial response by scanning the thin fluorescent sheet (made by a suspension of 40 nm microspheres) axially through the focal plane of the objective lens. The intensity is integrated over in-focus image after reconstruction using Equation (10). The relationships between the axial intensity distribution and the DMD pattern periods for two-beam and three-beam interference modes are shown in Figure 3a,b, respectively. Pattern periods were set from 5 to 30 pixels on the DMD. These pattern periods are equal to 3.5 to 21.1 μm for two-beam interference and 7.0 to 42.2 μm for three-beam interference in the sample plane. We found that the decreasing pattern period yields smaller axial FWHM, indicating that the finer pattern provides stronger optical sectioning capability. By correcting the effective light magnification β between the DMD plane and the sample plane, we obtained the quantitative comparison of the axial response, as shown in Figure 3c. The slight difference between the measured FWHMs and the theoretical FWHMs is properly due to the difficult estimation of the accurate light magnification β. To alleviate the impact of the inaccurate magnification, a plot of the axial FWHM response as a function of normalized spatial frequency is shown in Figure 3d. The measured FWHM of the axial response now agrees well with the theoretical FWHM. The slightly larger measured FWHM compared to theoretical FWHM at higher normalized spatial frequency is mainly due to the rapid intensity attenuation and fast degradation of pattern at higher normalized spatial frequency.

Figure 3c,d show how the equivalent FWHM for two-beam and three-beam interference modes can be achieved by adjusting the pixels per period and the spatial frequency. For example, for two-beam interference mode, the FWHM value of 23.1 μm can be achieved by setting 21 pixels per period on DMD and the corresponding normalized spatial frequency of 0.26. For three-beam interference mode, the approximate FWHM value of 22.8 μm can be achieved with the setting of 10 pixels per period on DMD, and the corresponding normalized spatial frequency of 0.27, which is close to the normalized spatial frequency of two-beam interference mode. For achieving the FWHM values of 13.2 μm and 13.4 μm for two-beam and three-beam interference modes, respectively, the corresponding setting of 6 pixels and 5 pixels per period on DMD is needed. The respective normalized spatial frequencies are 0.91 for two-beam interference mode and 0.54 for three-beam interference mode.

Next, we compared the optical sectioning performance between the two-beam and three-beam interference mode. We imaged a slice of mouse brain tissue. For fair comparison, all the exposure times of raw fringe images were set to 100 ms, and the pixel period were set to 21 pixels and 10 pixels for the two-beam and three-beam interference mode to provide approximate axial FWHMs, respectively. The SIM images obtained at the 75 μm beneath the surface are shown in Figure 4. In the three-beam SIM image (Figure 4b), the dendrites can be more easily resolved compared with that in the two-beam SIM image (Figure 4a). In the enlarged images (Figure 4c,d), some small features can be clearly identified in the three-beam SIM image (indicated by arrows) whereas they cannot be recognized in the two-beam SIM image. It should be noted that although extending the exposure time or increasing the laser power could increase the intensity of the image, the fine features of the dendrites cannot be observed in two-beam SIM images yet. These results demonstrate that the three-beam interference mode provides better optical sectioning capability and is more suitable for imaging thick biological tissues than the two-beam interference mode. The reasons are not fully understood but they are believed to be largely due to the greater modulation contrast provide by three-beam interference as illustrated in the Theory section.

According to the previous study [17], the greater modulation contrast provides better optical sectioning.

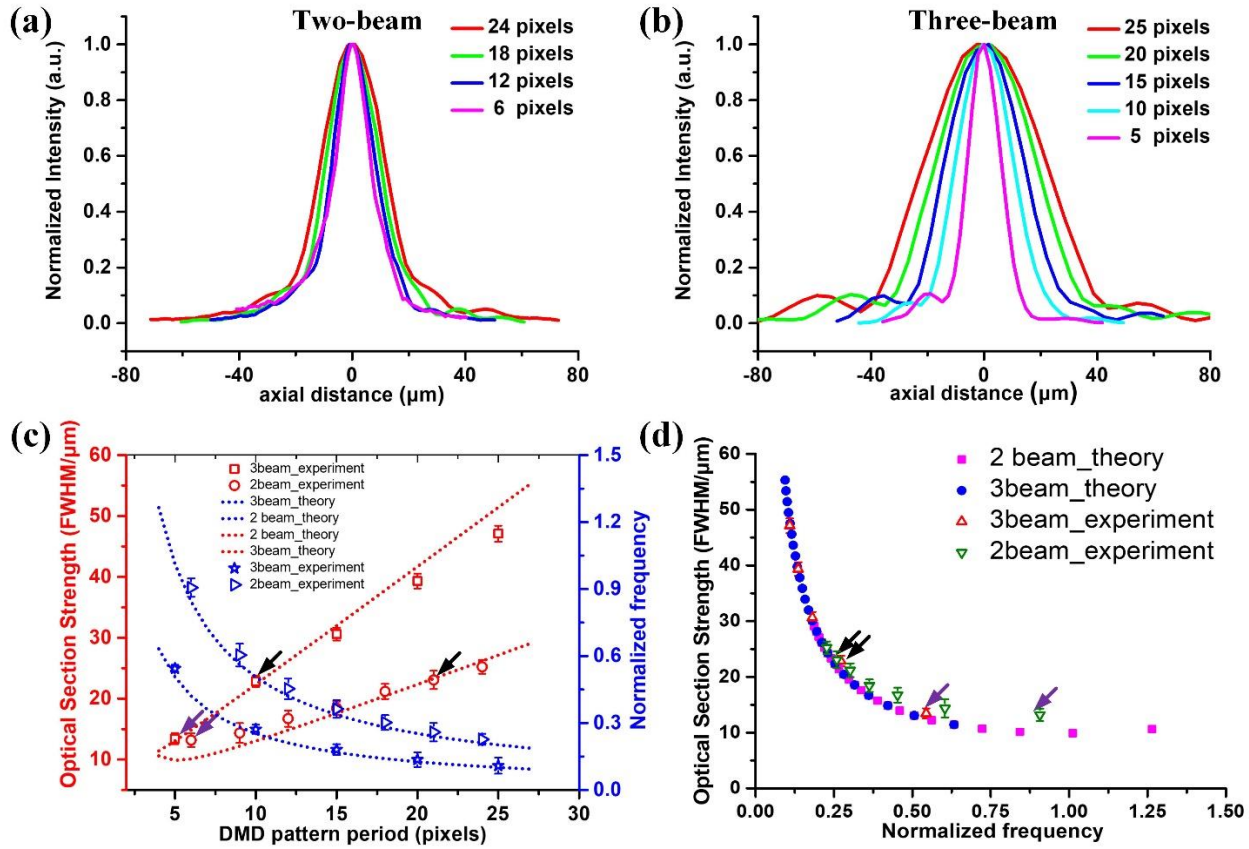

Figure 3. Axial responses at various pattern periods for two-beam (**a**) and three-beam (**b**) interference modes. (**c**) The measured and theoretical FWHMs of the axial response and normalized frequency present as a function of pattern periods for two-beam (red circle and blue triangle) and three-beam interference modes (red square and blue star). (**d**) The measured and theoretical FWHMs present as a function of normalized spatial frequency for two-beam (green triangle) and three-beam interference modes (red diamond).

4.2. Two-Beam Interference Mode Provides Fast Imaging Capability

The two-beam interference mode theoretically provides higher imaging speed because of the less numbers of phase shifts needed to form the image. To demonstrate the fast imaging capability using our DMD-SIM, we developed an optical flow phantom model. The injected fluorescent microspheres move rapidly and independently under the control of a micro-syringe pump in this model. The experimental ROI of all recorded images are set to 256 × 256 pixels and 1 × 1 binning (corresponding to the field of view of 149.76 μm × 149.76 μm). Figure 5 shows the optical sectioning and wide-field image of fast-moving fluorescent microspheres over 300-time points. For the two-beam interference mode, our system achieves a raw frame rate of 200 frames per second, resulting in an optical sectioning frame rate of 66.6 Hz (three-step phase-shifting). It is clear that the stationary microspheres pointed by blue arrows are mostly excluded in optical sectioning images but are apparent in wide-field images. The same result also has been observed for the moving microspheres pointed by blue squares. The mean flowing speed of the moving microsphere indicated by the white arrow is calculated to be 18.8 μm/s through the traveling length of 144.4 pixels and traveling time of 4.5 s.

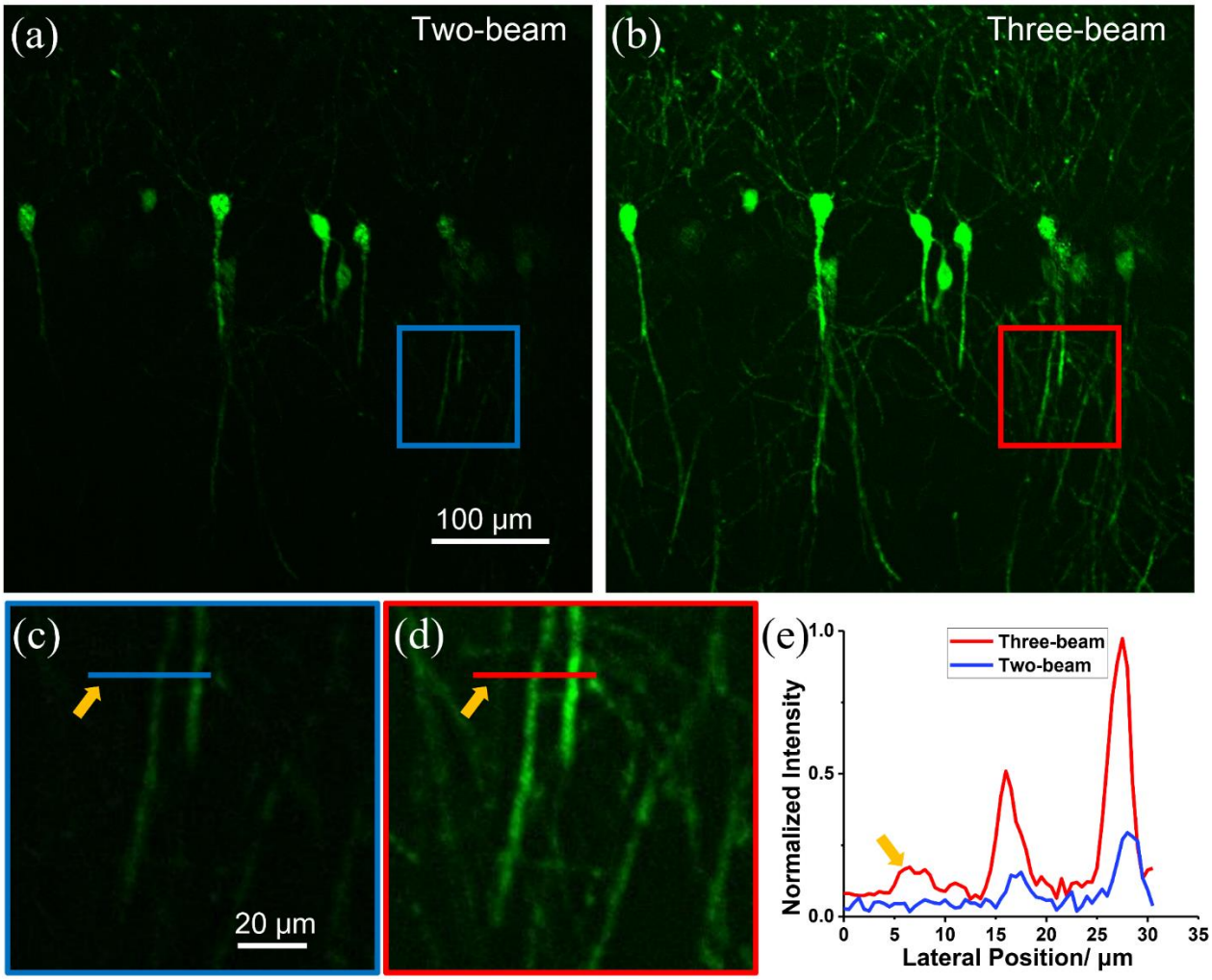

Figure 4. SIM images of brain tissue section acquired by two-beam illumination (**a**) and three-beam illumination (**b**). (**c**,**d**) Magnification images of the solid rectangles in (**a**,**b**). (**e**) The cross-sectional intensity profiles along the dendrites indicated by the solid lines in (**c**,**d**). All images were normalized to the maximum gray value of the two-beam interference SIM image.

For investigating the fastest imaging speed of our DMD-SIM system for different fields of view, the active ROI of the camera is set differently and the camera exposure time is kept to a minimum (1 ms) so that the system can operate at its maximum speed. Our system could achieve a maximum optical sectioning frame rate of up to 135.1 Hz (256 × 256 pixels with 1 × 1 binning) (see Table 1). By contrast, the SIM imaging on three-beam interference mode can only reach a frame rate of 81 Hz. It should be noted that the lower exposure time will result in a low signal-to-noise ratio (SNR) and yield poor image contrast. It is important to use optimum exposure time (10 ms–30 ms) to provide sufficient contrast for biological experiments.

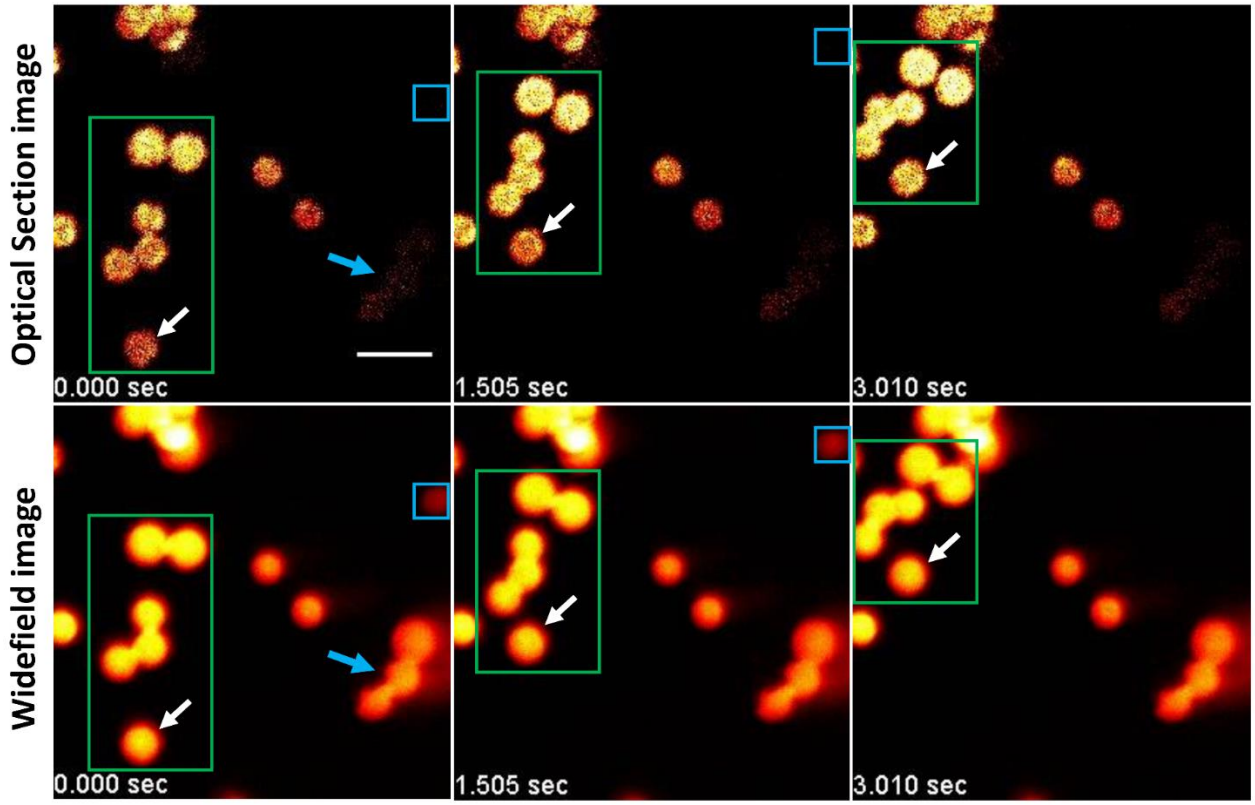

Figure 5. Fast imaging of moving fluorescent microspheres; blue arrows point to the stationary microspheres, and different squares point to the moving microspheres, scale bar: 30 μm.

Table 1. Acquisition raw frame rate and one optical-sectioning SIM frame rate according to different ROIs.

ROI Pixel	Binning	Effective Pixel	DMD Exposure Time (ms)	Times @ Images	Raw Frame (fps)	Restore Frame (fps)
2048 × 2048	2 × 2	1024 × 1024	11	6.72 s @ 600 p	89.3	29.7
1024 × 1024	2 × 2	512 × 512	6	3.72 s @ 600 p	161.3	53.7
512 × 512	1 × 1	512 × 512	3.5	2.22 s @ 600 p	270.3	90.1
256 × 256	1 × 1	256 × 256	2.26	1.48 s @ 600 p	405.4	135.1

External edge trigger mode/sCMOS exposure time: 1 ms/two-beam interference mode.

4.3. Three-Beam Interference Mode Provides Great Volumetric Imaging Capability

To demonstrate the feasibility of the three-beam interference mode of DMD-SIM for volumetric biological imaging, we imaged an optical cleared mouse brain tissue. We achieved an imaging depth of up to 300 μm. The maximum intensity projections (MIP) of different stack of the captured volume are shown in Figure 6. We found that the single neuronal structure in the cortex at deeper depth can still be recognized. The lateral field-of-view of each optical sectioning image was 394 μm×394 μm, and each image was scanned at 1 μm interval in optical direction. The 300 μm thick, volumetric imaging of clearing brain tissue was accomplished in approximately 75 s. Of these 75 s, only 15 s were used for imaging acquisition time. The remaining 60 s were spent in moving the motorized translation stage between successive frames (it took about 200 ms between two successive stages).

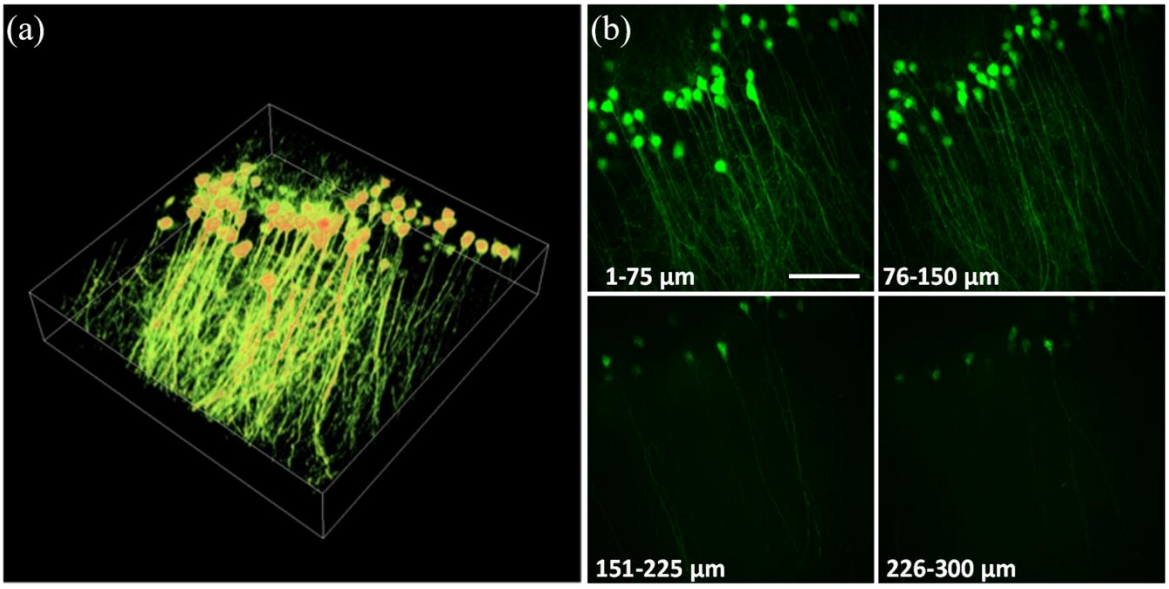

Figure 6. Volumetric imaging of the cleared brain tissue section. (**a**) Three-dimensional image of the cleared brain tissue section. (**b**) MIP of different stack of the captured volume, scale bar: 100 µm.

5. Discussion and Conclusions

In this study, we systematically compared benefits of pattern generation between two-beam and three-beam interference in SIM system. The measured FWHMs of the axial response with respect to pattern periods using a home-built DMD-SIM were in agreement with the theoretical prediction. In the two-beam interference mode, the fastest imaging speed achieved was up to 135.1 fps. We demonstrated the fast optical sectioning imaging capability by imaging the flow-phantom model. We also presented large volumetric biological imaging using the three-beam interference mode in mouse brain tissue. The maximum penetration depth achieved in the mouse brain section was up to 300 µm.

In the past few years, several methods were proposed to increase the imaging speed of SIM. Santos et al. proposed a method called HiLo SIM to construct the optical sectioning image using only two exposures of grid-pattern illumination and uniform illumination [18]. Hoffman et al. further reduced the exposure number. They used Hilbert transform demodulation to produce the sectioning image with a single modulated image [19]. Wang et al. presented another method to construct a sectioning image based on a single-shot exposure [20]. In their method, a filter in the Fourier domain is used to obtain a fringe-free spectrum, and the reconstructed image is recovered from its inverse Fourier transform and modulus calculations. All these methods can reduce the exposure times, thereby increasing the imaging speed. It is worth noting that all these methods could be transplanted to our system, because the DMD used in our system can flexibly generate illumination patterns.

Except the simple two-beam or three-beam interference used in this study, other novel methods were proposed in recent years to generate the modulation illumination patterns. Pal et al. revealed that the polarization lattice structure can be generated by the interference of three linearly polarized non-coplanar plane waves [21]. Further, they proved that if the beam polarization is properly designed, the fringe contrast can be significantly improved [22]. Chen and colleagues used a segmented half-wave plates to change the polarization of two interference beams to produce high contrast fringe patterns [4]. Recently, Xu et al. used asymmetric three-beam interference to generate the modulation illumination patterns, avoiding the zero-order diffracted light whose polarization cannot be changed using a static six-sector half-wave plate [23]. Shabani et al. proposed an interesting approach to generate three-dimensional modulation illumination patterns [24]. This method is based on the incoherent illumination of a Fresnel biprism using several equidistant linear sources. They demonstrated that as the number of slits increases,

the axial confinement of the pattern increases, and the system's optical sectioning capability also improves. All these methods can produce modulated illumination patterns; therefore, they can be used to obtain sectioning images. However, the systematic comparison of the optical sectioning capability between these methods is beyond the scope of this study and may be our future research goal.

In summary, in this study we found that the two-beam interference mode is suitable for fast imaging of thin samples and the three-beam interference mode is applicable to imaging the thick and deeper samples. We hope that these results and analysis could provide guidance to the researchers in choosing the appropriate multi-beam interference in DMD-SIM for their specific applications. In future, we will combine the new fringe pattern generation method, such as the polarization lattice structure, with the single-shot reconstruction algorithm, such as the Hilbert transform demodulation to increase the imaging speed as well as improve the sectioning capability of SIM. Additionally, we will extend our study to systematically compare the interference patterns generated by asymmetric diffraction orders beams [23].

Author Contributions: Conceptualization, J.L.; methodology, L.L. and X.X.; writing—original draft preparation, J.L. and T.C.; writing—review and editing, H.L. and W.Z.; supervision, W.Z. All authors have read and agreed to the published version of the manuscript.

Funding: This research was funded by the National Key Research and Development Program of China, (2017YFC0110200); the National Natural Science Foundation of China (81822023, 91959121, 82071972, 82102106); the Guangdong Basic and Applied Basic Research Foundation (2019A1515011746, 2020B121201010); the Scientific Instrument Innovation Team of the Chinese Academy of Sciences (GJJSTD20180002); and the Shenzhen Basic Research Program (JCYJ20180507182432303, RCJC20200714114433058, ZDSY20130401165820357).

Institutional Review Board Statement: All animal procedures were carried out in compliance with the laboratory animal protocols approved by the Institutional Animal Care and Use Committee of the Shenzhen Institutes of Advanced Technology, Chinese Academy of Sciences (No. SIAT-IACUC-200818-YGS-LJL-A1375, 19 August 2020).

Informed Consent Statement: Not applicable.

Data Availability Statement: Data are available from the authors upon request.

Conflicts of Interest: The authors declare no conflict of interest.

References

1. Webb, R.H. Confocal optical microscopy. *Rep. Prog. Phys.* **1996**, *59*, 427–471. [CrossRef]
2. Helmchen, F.; Denk, W. Deep tissue two-photon microscopy. *Nat. Methods* **2005**, *2*, 932–940. [CrossRef]
3. Stelzer, E.H.K. Light-sheet fluorescence microscopy for quantitative biology. *Nat. Methods* **2015**, *12*, 23–26. [CrossRef]
4. Huang, X.; Fan, J.; Li, L.; Liu, H.; Wu, R.; Wu, Y.; Wei, L.; Mao, H.; Lal, A.; Xi, P.; et al. Fast, long-term, super-resolution imaging with Hessian structured illumination microscopy. *Nat. Biotechnol.* **2018**, *36*, 451–459. [CrossRef]
5. Wu, Y.; Shroff, H. Faster, sharper, and deeper: Structured illumination microscopy for biological imaging. *Nat. Methods* **2018**, *15*, 1011–1019. [CrossRef] [PubMed]
6. Gustafsson, M.G.L. Surpassing the lateral resolution limit by a factor of two using structured illumination microscopy. *J. Microsc.* **2000**, *198*, 82–87. [CrossRef] [PubMed]
7. Li, M.; Li, Y.; Liu, W.; Lal, A.; Jiang, S.; Jin, D.; Yang, H.; Wang, S.; Zhanghao, K.; Xi, P. Structured illumination microscopy using digital micro-mirror device and coherent light source. *Appl. Phys. Lett.* **2020**, *116*, 233702. [CrossRef]
8. Zhuang, Z.; Ho, H.P. Application of digital micromirror devices (DMD) in biomedical instruments. *J. Innov. Opt. Health Sci.* **2020**, *13*, 2030011. [CrossRef]
9. Dan, D.; Lei, M.; Yao, B.; Wang, W.; Winterhalder, M.; Zumbusch, A.; Qi, Y.; Xia, L.; Yan, S.; Yang, Y.; et al. DMD-based LED-illumination Super-resolution and optical sectioning microscopy. *Sci. Rep.* **2013**, *3*, 1116. [CrossRef] [PubMed]
10. Xu, D.; Jiang, T.; Li, A.; Hu, B.; Feng, Z.; Gong, H.; Zeng, S.; Luo, Q. Fast optical sectioning obtained by structured illumination microscopy using a digital mirror device. *J. Biomed. Opt.* **2013**, *18*, 060503. [CrossRef]
11. Gustafsson, M.G.L.; Shao, L.; Carlton, P.M.; Wang, C.J.R.; Golubovskaya, I.N.; Cande, W.Z.; Agard, D.A.; Sedat, J.W. Three-Dimensional Resolution Doubling in Wide-Field Fluorescence Microscopy by Structured Illumination. *Biophys. J.* **2008**, *94*, 4957–4970. [CrossRef]

12. Dan, D.; Yao, B.; Lei, M. Structured illumination microscopy for super-resolution and optical sectioning. *Chin. Sci. Bull.* **2014**, *59*, 1291–1307. [CrossRef]
13. Chang, B.-J.; Tang, W.-C.; Liu, Y.-T.; Tsai, Y.-C.; Tsao, C.; Chen, P.; Chen, B.-C. Two-beam interference lattice lightsheet for structured illumination microscopy. *J. Phys. D Appl. Phys.* **2020**, *53*, 044005. [CrossRef]
14. Doblas, A.; Shabani, H.; Saavedra, G.; Preza, C. Tunable-frequency three-dimensional structured illumination microscopy with reduced data-acquisition. *Opt. Express* **2018**, *26*, 30476–30491. [CrossRef]
15. Neil, M.A.A.; Juškaitis, R.; Wilson, T. Method of obtaining optical sectioning by using structured light in a conventional microscope. *Opt. Lett.* **1997**, *22*, 1905–1907. [CrossRef]
16. Neil, M.A.A.; Juškaitis, R.; Wilson, T. Real time 3D fluorescence microscopy by two beam interference illumination. *Opt. Commun.* **1998**, *153*, 1–4. [CrossRef]
17. Zhanghao, K.; Liu, W.; Li, M.; Wu, Z.; Wang, X.; Chen, X.; Shan, C.; Wang, H.; Chen, X.; Dai, Q.; et al. High-dimensional super-resolution imaging reveals heterogeneity and dynamics of subcellular lipid membranes. *Nat. Commun.* **2020**, *11*, 5890. [CrossRef]
18. Silvia, S.; Kengyeh, K.C.; Daryl, L.; Nenad, B.; Timothy, N.F.; Claire, H.; Aaron, C.B.; Satish, K.S.; Jerome, M. Optically sectioned fluorescence endomicroscopy with hybrid-illumination imaging through a flexible fiber bundle. *J. Biomed. Opt.* **2009**, *14*, 030502. [CrossRef]
19. Zachary, R.H.; Charles, A.D. Single-image structured illumination using Hilbert transform demodulation. *J. Biomed. Opt.* **2017**, *22*, 056011. [CrossRef]
20. Wang, H.; Liu, W.; Hu, Z.; Li, X.; Hong, B. One-shot optical sectioning structured illumination microscopy. In Proceedings of the Applied Optics and Photonics China (AOPC2019), Beijing, China, 7–9 July 2019.
21. Pal, S.K.; Senthilkumaran, P. Cultivation of lemon fields. *Opt. Express* **2016**, *24*, 28008–28013. [CrossRef] [PubMed]
22. Pal, S.K.; Senthilkumaran, P. Lattice of C points at intensity nulls. *Opt. Lett.* **2018**, *43*, 1259–1262. [CrossRef] [PubMed]
23. Xu, L.; Zhang, Y.; Lang, S.; Wang, H.; Hu, H.; Wang, J.; Gong, Y. Structured illumination microscopy based on asymmetric three-beam interference. *J. Innov. Opt. Health Sci.* **2020**, *14*, 2050027. [CrossRef]
24. Shabani, H.; Doblas, A.; Saavedra, G.; Sanchez-Ortiga, E.; Preza, C. Improvement of two-dimensional structured illumination microscopy with an incoherent illumination pattern of tunable frequency. *Appl. Opt.* **2018**, *57*, B92–B101. [CrossRef] [PubMed]